Supplementary Information

Andean volcanism, ocean fertilization, marine ecosystem turnover, and global cooling in the Late Miocene

Barbara Carrapa[1†], Mark Clementz[2], Nicolás J. Cosentino[3,4,5], Pedro Di Nezio[6], Pam Vervoort[7], Kaustubh Thirumalai[1], Jordan T. Abell[8], Dominik Hülse[9], Priscilla R. Martinez[1], Carolina Gutstein[10]

[†]e-mail: bcarrapa@arizona.edu

Supplementary Note 1. Ash plume simulations with Hysplit 5.3.0

Model description and configuration

HYSPLIT 5.3.0 (Hybrid Single-Particle Lagrangian Integrated Trajectory (1) is an atmospheric transport and dispersion model used to simulate the trajectories, dispersion, and deposition of airborne particles, gases, and pollutants. We ran particle dispersion simulations with Hysplit 5.3.0 to derive the present-day spatial distribution of ash deposition from volcanic eruptions in the Puna-Altiplano region. Atmospheric advection and diffusion were calculated based on the NCEP/NCAR Reanalysis I, with temporal and spatial resolutions of 6 h and 2.5º, respectively. Dry deposition occurs by gravitational settling, and the (2) formulation was used to calculate non-spherical particle fall speeds. Wet deposition was modeled as both below-cloud and in-cloud scavenging, for which default efficiency parameter values were used (both 8×10^{-5} s^{-1}). To derive a representative ash mass emission rate for Late Miocene eruptions, we used the average ignimbrite volume eruption rate between 7.5-5.5 Ma for the Cerro Galan and southern half of the Altiplano-Puna volcanic zone (APVC; 18.4 km^3 10^{-4} yr^{-1}; (3)), the median density of ignimbrite-forming pyroclastic density currents (PDC) of 1980-2019 eruptions (1770 kg m^{-3}; (4)), and the median ash-to-PDC mass ratio of 1980-2019 eruptions (2.1; (5)). Finally, a correction (x1.32) was applied to consider the full extent of the Cerro Galan plus APVC ignimbrite volume, which, based on previous estimates, ranges between 16,500-17,300 km^3 ((6); (7, 8)). This gives a mean ash emission rate of 90.3 Pg 10^{-4} yr^{-1}. We assumed this total mass was emitted by multiple VEI6-type explosive volcanic eruptions with a 75-year recurrence. The recalculated ash mass for each eruption was emitted from multiple points along a vertical line from 100 m to 15.7 km above the crater (23.5ºS, 67.5ºW), during one week at a constant rate. Simulated ash transport and deposition persisted for four days after the end of emissions.

We parameterized the grain size distribution of volcanic ash aerosols at emission based on the detailed measurements available for the 2008 Chaitén eruption in Chile (9). This distribution consists of six grain size populations, each with a central-value grain size of 2.4 μm, 12.5 μm, 31.3 μm, 89.5 μm, 415.1 μm and 4254 μm. The mass apportionment was modified compared to that of (9) to reflect the fact that extremely explosive volcanic eruptions generate ash aerosols where 50% of the mass is in particles below 63 μm (eruption categories S3 and S8 of (10)). The resulting mass apportionment is: 6.7%, 21.1%, 22.3%, 22.9%, 22.8% and 4.3%, for grain size populations #1-6, respectively. Finally, to create a realistic, continuous grain size distribution, each population was additionally subdivided into 10 sub-populations, with mass apportioned so that the cumulative mass distribution with respect to the base-10 logarithm of the particle diameter is linear between

the central-value grain sizes of two contiguous populations. Particle density was set at 2242 kg m^{-3}, based on measurements on ash from the 2008 Chaitén eruption (11). Particle shape was set assuming a sphericity (i.e., between 0 and 1, with a value of one representing a sphere) of 0.8 (e.g., (12)). To derive a representative ash plume that averages out seasonal and interannual variabilities, we simulated one event during each month for 10 years (January 2014-December 2023), with emissions starting at 0.00 hs UTC of the first day of each month. In Supplementary Figure 1 the monthly climatology of ash deposition is shown. We used the mean ash deposition field as input for the biogeochemical simulations.

Nutrient flux estimation

We estimated the flux of ash-derived nutrients, phosphorus (P), iron (Fe), and silica (Si), based on the mean field of ash deposition, the content of nutrients of ash, and the fraction of nutrients in ash that is soluble (i.e., bioavailable). We set the total Fe content in ash as 3.5% (e.g., (13)) while the solubility of Fe depended on the ratio of coarse-to-fine ash deposition, with higher values of Fe solubility for finer ash. This is equivalent to how non-volcanic mineral dust Fe solubility is implemented in MARBL, the ocean biogeochemistry component of CESM, and is based on (14). The mean Fe solubility (i.e., fraction of total Fe that is soluble) in deposited ash turned out to be 27.3% . In turn, the mass fraction of soluble Si and of soluble P with respect to total ash was set to 2.3% and 0.016%, respectively. In all cases (Fe, Si, and P), the soluble contents of these elements with respect to the total mass of deposited ash were within the lower half of available estimates for Andean ash (Fe: 0.001-0.02%, P: 0.00001-0.01%, Si: 0.01-0.1%; (15-19).

Supplementary Note 2. Short-term productivity simulations with CESM

Model description and configuration

We simulated the response of ocean ecosystems and the carbon (C) cycle to pulses of nutrients associated with volcanic ash using the low-resolution configuration of the Community Earth System Model (CESM) version 2.1.5 (20). This configuration of CESM provides a realistic representation of the climate system (21), and the marine carbon cycle (22). CESM includes an ocean biogeochemical component, MARBL (23), capable of simulating ocean biogeochemistry, including C, nitrogen, P, Fe, Si, and oxygen, as well as ecosystem dynamics. MARBL includes one zooplankton group, three explicit phytoplankton functional groups (diatoms, diazotrophs, "small" pico/nano phytoplankton), and one implicit group (calcifiers). In addition, it simulates 32 tracers, comprising 17 non-living constituents (dissolved inorganic C, alkalinity, nutrients, oxygen, and dissolved organic matter) and 15 tracers associated with living biomass (i.e., phytoplankton C, P, Si, Fe, $CaCO_3$ and zooplankton C). Carbonate chemistry is explicit, including DIC and alkalinity tracers. In terms of nutrients, phytoplankton productivity was modeled to depend on Si, Fe and P. The ocean component, POP2, was configured with a resolution of 2° latitude × 4° longitude (lowering to less than 2° latitude resolution in the Southern Ocean), and 60 vertical levels (24). POP2 represents subgrid-scale processes, such as mesoscale and submesoscale processes, including a variable eddy-induced advection coefficient (25), which improves realism of eddy-driven mixing of carbon in the Southern Ocean at coarse resolution (26). The atmospheric component, CAM4, was configured with a horizontal resolution of ~3.75° × 3.75° and 26 vertical levels (27), providing a realistic simulation of large-scale atmospheric circulation patterns (22).

CESM was configured with non-interactive atmospheric CO_2. In this configuration the model simulates a fully prognostic ocean carbon cycle, but changes in air-sea CO_2 fluxes do not affect atmospheric CO_2 concentrations, which remain constant at 284.7 ppm. We performed a control simulation for a 1300-year period with constant boundary conditions to obtain quasi-equilibrated ocean circulation and carbon cycle states as baseline for our "ash fertilization" simulation. Modern boundary conditions are used to compute the climate. CESM derives ocean nutrients from multiple sources (including non-volcanic mineral dust aerosols emitted from deserts). In our control simulation, these dust and dust-borne nutrient fluxes exhibit large-scale patterns dominated by atmospheric transport from deserts. Ash-derived nutrient fluxes were not included in this control simulation. Over the last 400 years of the control simulation, the globally integrated air-sea CO_2 flux approaches zero (-0.07 PgC yr^{-1}), consistent with an equilibrated carbon cycle.

Experimental design

We simulate the response of ocean ecosystems and carbon cycling to Andean volcanism by applying a series of pulses of nutrients to our CESM control simulation. Four pulses were applied in a span of 300 years, each during a different month (December, March, June, and September) to explore whether the ecosystem responses are sensitive to the seasonal timing of volcanic eruptions. We do not explore the sensitivity of other major uncertainties, such as the content of nutrients in ash and their solubility (i.e., bioavailability). Last, our modelling approach does not consider the radiative effect of volcanic aerosols, which could impact marine productivity via changes in available sunlight or temperature. Each pulse of nutrients is applied every 75 years based on the ash plume calculations performed with Hysplit. Each pulse lasts a month, during which fluxes of Fe, P, and Si are added to the climatology of the model at different calendar months. The first pulse was applied in December of the year 1001 to maximize the impact on the response of marine ecosystems in the Southern Hemisphere. Subsequent pulses were applied in March of the year 1076, June of the year 1151, and September of the year 1226 to consider alternative fertilization seasons. The resulting simulation provides an idealized representation of a 300-year interval with four pulses of nutrients every 75 years.

Supplementary Note 3. Long-term carbon cycle simulations with cGENIE

Model description and configuration

The cGENIE Earth system model of intermediate complexity consists of a 3D frictional geostrophic ocean circulation model coupled to a 2D energy moisture balance model and a thermodynamic sea ice model (28). A biogeochemical module resolves the biogeochemical reactions in the ocean and atmosphere while tracking a multitude of tracers (29). Particulate organic (POC), particulate inorganic carbon ($CaCO_3$), organic-bound phosphorus (POC-P), and organic-bound iron (POC-Fe) are produced in the surface ocean with the ratio of $CaCO_3$ to POC export productivity linked to the calcite saturation state of surface waters. In the set-up used here, marine biological productivity is limited by light availability and co-limited P and Fe, but not by Si. Si is crucial for diatoms–the most prevalent group of primary producers in the Southern Ocean–but the Southern Ocean generally contains plenty of dissolved Si in the modern system, leaving Fe as the nutrient controlling primary productivity in this region (30). Dissolved Fe in cGENIE is present in free (Fe^{3+}) or ligand-bound form, both can be consumed by primary producers but only Fe^{3+} can be scavenged by POC (31-33). The rate of scavenging increases with the POC export flux

and thus constitutes a negative feedback: an increase in Fe availability raises POC export and accelerates the scavenging and removal of Fe from the ocean. Most POC that sinks through the water column is remineralized, releasing Fe^{3+} and PO_4 back to the ocean, except for a small fraction that reaches the seafloor. All POC-Fe particles that escape water column remineralization are buried (31) so are decoupled from simulated POC burial rates that vary as a function of the POC flux to the seafloor (34). The burial of POC-P is coupled to POC burial and occurs in a 106:1 Redfield ratio under oxic conditions. Preferentially more POC-P is remineralized over POC in regions where benthic oxygen concentrations fall below 120 μmol kg^{-1} (35, 36). The $CaCO_3$ burial rate depends on the saturation state of overlying waters (37). Buried C and P are replenished via inputs from fixed rates of terrestrial weathering of silicate, carbonate, kerogen, and phosphate-bearing rocks and volcanic CO_2 outgassing (35, 38). A spatially-explicit dust field is prescribed to replenish Fe, assuming 3.5% of the total dust flux constitutes Fe with a variable percentage thereof being soluble Fe available for consumption. The soluble Fe percentage varies as a function of the local dust flux.

Simulations are performed under modern boundary conditions (39) to match the CESM simulations for direct comparison. The model is spun up to pCO_2 at 278 μatm, ocean alkalinity of 2363 μmol kg^{-1} and dissolved inorganic carbon pool of 2241 μmol kg^{-1} with dust fields obtained from (40). This results in a global mean surface temperature of 12.4°C with global $CaCO_3$ and POC export fluxes of 0.84 PgC yr^{-1} and 6.26 PgC yr^{-1}, respectively. The distribution of nutrients available at the surface is driven by ocean circulation generating regions of PO_4-limitation in the ocean gyres and regions of Fe-limitation in major upwelling zones (Supplementary Figure 2). Consistent with observations, most POC export occurs in the high latitude northern and southern oceans and in equatorial upwelling zones (Supplementary Figure 3). The ocean saturation state drives a global $CaCO_3$ burial flux of 0.14 PgC yr^{-1}. A 5x scaling is applied to the POC burial relationship to produce a global deep ocean POC burial flux of 0.06 PgC yr^{-1} to approximate modern estimates (41).

Experimental design

To evaluate how Andean volcanism and aridification influenced marine primary productivity and carbon cycling on millennial timescales and longer, we follow the same procedure as the CESM simulations (Supplementary Note 2). We apply a series of spatially-explicit nutrient fluxes to the surface ocean. These fields are regridded from the Hysplit ash plume flux model (Supplementary Note 1), using only the soluble fraction of Fe and PO_4. Whereas in CESM the nutrient fluxes are applied over the span of a month, the fluxes in cGENIE are applied over the span of a year while maintaining the same total nutrient flux as in CESM, resulting in a more diluted but year-long flux of 0.719 Tmol Fe yr^{-1} and 0.021 Tmol PO_4 yr^{-1} for a single pulse. Except for Experiment 4, these values are scaled depending on the frequency of pulses so the long-term average flux is always the same. We run a total of four 20-kyr long simulations.

1. One (33.3%) Fe-PO_4 ash flux every 25 yr
2. One (100%) Fe-PO_4 ash flux every 75 yr
3. One (200%) Fe-PO_4 ash flux every 125 yr
4. One (1200%) Fe-PO_4 ash flux every 75 yr
5. One (100%) Fe-PO_4 ash flux every 75 yr plus double dust Fe solubility

Experiments 1, 2, and 3 are designed to study how the frequency of volcanic eruptions impacts the Earth system response to nutrient fertilization (Supplementary Figure 4). We particularly focus on

the influence of ocean dynamics in the redistribution of carbon and nutrients in these millennial-scale experiments. Experiment 4 is used to evaluate the impact of temporarily elevated volcanic ash plume emissions. The majority of volcanic eruptions occurred in three concentrated intervals during separate phases in the formation of the APVC. The ash production rates increased during these periods, reaching up to 12 times the long-term average rate during the first phase at 8.4 Ma (42). We assume that the total marine ash deposition and related nutrient input scale linearly with the volcanic ash eruption while the area of deposition remains the same. Experiment 5 is forced with repeated nutrient fluxes but also receives additional soluble Fe input to represent a global increase in dust-derived Fe (e.g (43)). This is achieved by doubling the percentage of aeolian Fe solubility. The actual change in aeolian derived fluxes across the Miocene in response to aridification is uncertain. This rather arbitrarily chosen increase in solubility is intended to demonstrate the combined impact of dust and ash inputs in a qualitative manner but note that a doubling in the solubility falls within a reasonable range that is comparable to the difference in dust solubility between more recent interglacial and glacial periods (44).

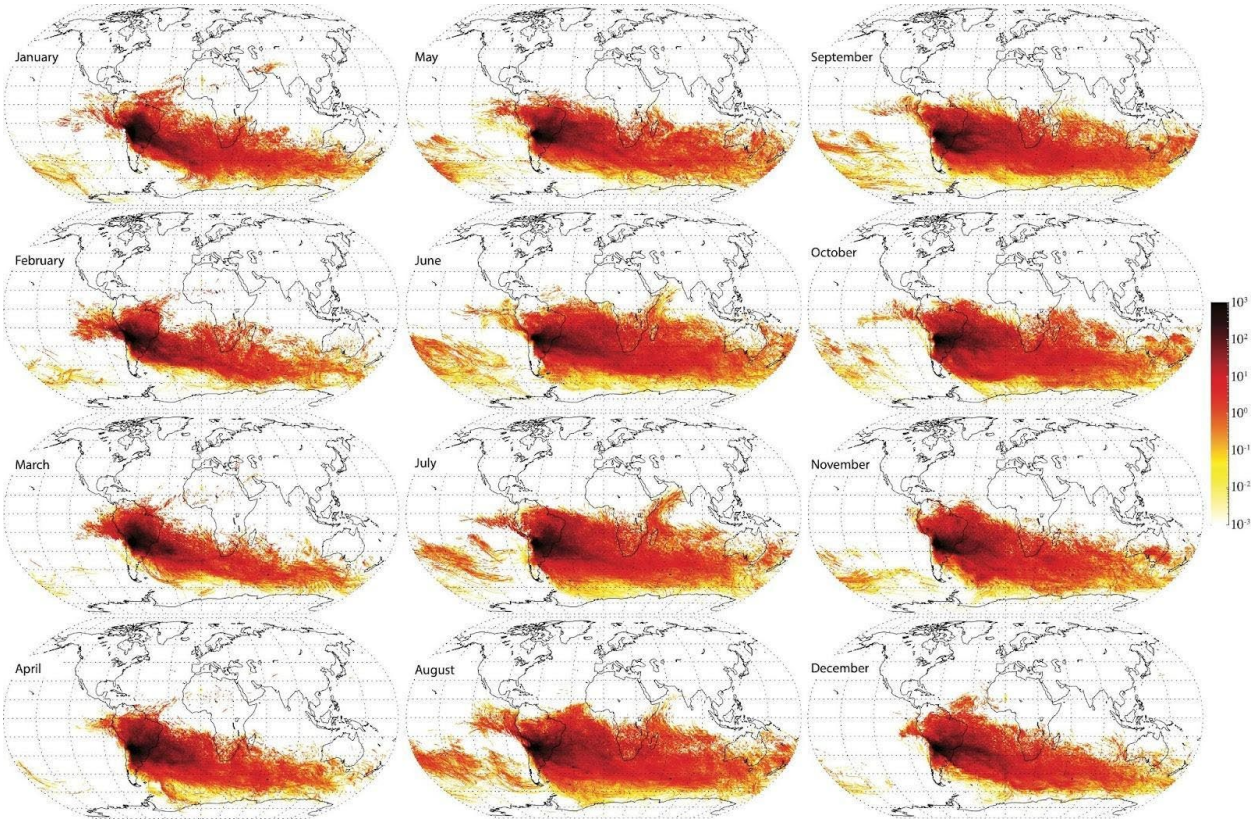

Supplementary Figure 1. Monthly climatology (2014-2023) of simulated total bulk ash deposition (g m^{-2}).

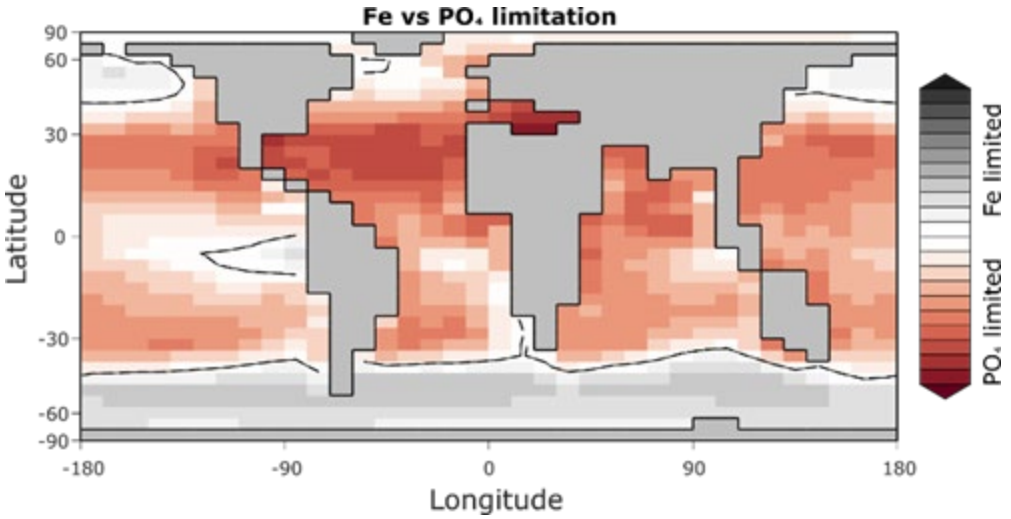

Supplementary Figure 2. Regions of iron (Fe) versus phosphate (PO_4) limitation in the cGENIE Earth system model. Under modern boundary conditions, primary productivity in most of the open ocean is limited by macronutrient PO_4 in the oligotrophic waters of the ocean gyres (red). In regions of upwelling such as the southern oceans, North Pacific, and equatorial zone, macronutrients are readily replenished as nutrient-rich deep waters resurface but primary productivity is limited by micronutrient Fe (grey).

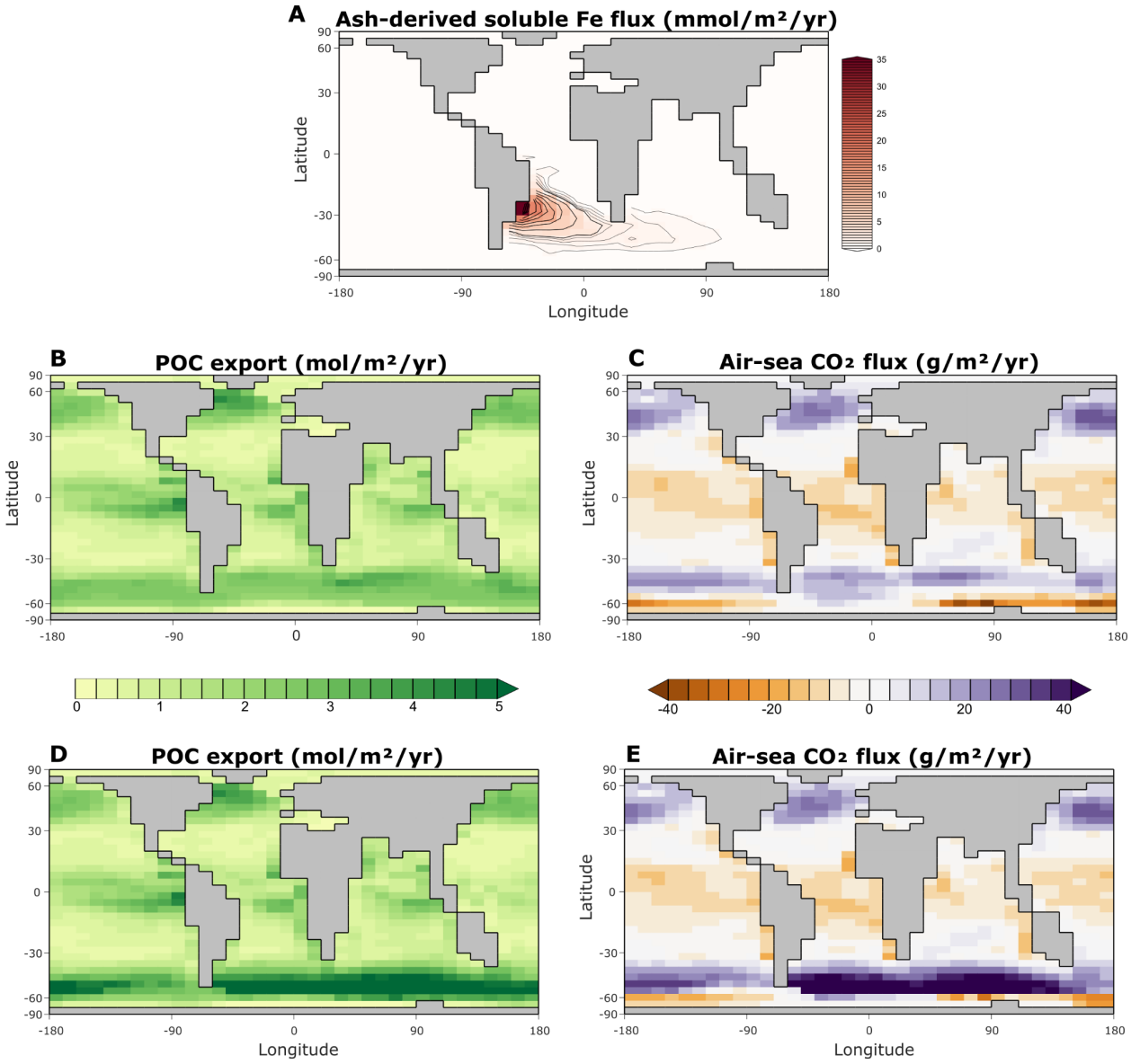

Supplementary Figure 3. Simulated ash-derived iron flux associated with Andean volcanism and the response of primary productivity and air-sea CO_2 exchange in cGENIE. A. The ash-derived Fe flux associated with volcanism in the Puna/Altiplano region (APVC). This flux in cGENIE is imposed as an annual mean flux with a magnitude and distribution consistent with that applied in CESM where the ash flux is imposed as a monthly flux. B & C. Simulated annual mean particulate organic carbon (POC) surface export and air-sea CO_2 flux of the control simulation without ash fertilization. D. & E. Simulated annual mean POC surface export and air-sea CO_2 flux after a year-long pulse of nutrients. The model simulates a noticeable increase in POC surface export and CO_2 flux into the ocean in response to the pulse of nutrients delivered by ash.

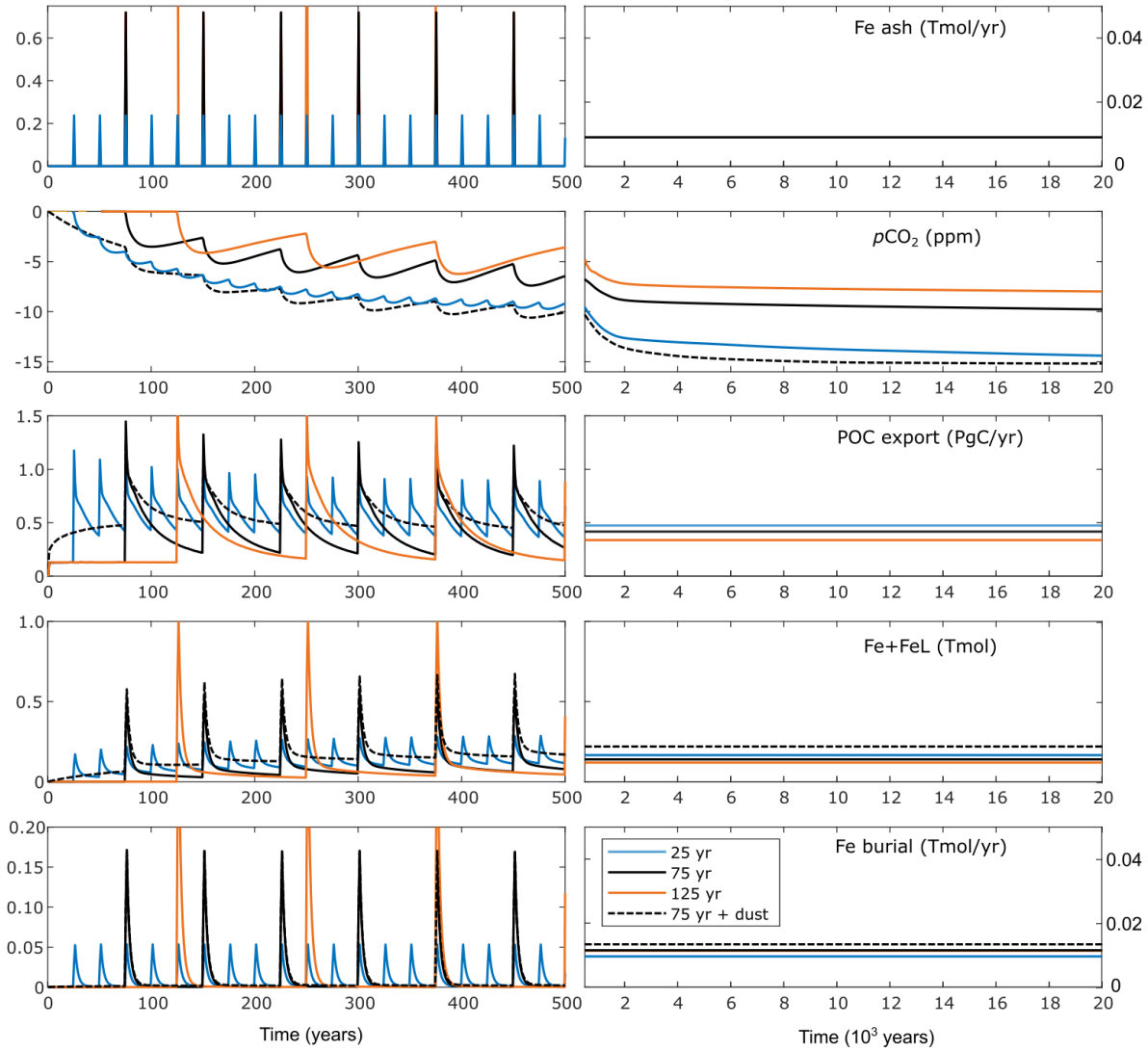

Supplementary Figure 4. cGENIE model time series of (A) Total global ash Fe flux (Tmol/yr), (B) Global mean change in pCO_2 (µatm), (C) Global annual mean change in surface POC export (PgC/yr), (D) Total ocean dissolved iron pool, sum of free iron (Fe^{3+}) and ligand-bound iron (FeL) (Tmol), and (E) Global annual mean Fe burial (Tmol/yr). Simulations that test the impact of eruption frequency and enhanced dust emissions are shown. In steady-state, the global mean Fe burial flux is equal to the aeolian Fe input (not shown) and Fe input from ash shown in panel A.

Supplementary References

1. A. F. Stein *et al.*, NOAA's HYSPLIT atmospheric transport and dispersion modeling system. *Bulletin of the American Meteorological Society* **96**, 2059-2077 (2015).
2. G. H. Ganser, A rational approach to drag prediction of spherical and nonspherical particles. *Powder technology* **77**, 143-152 (1993).
3. D. Bertin *et al.*, Magmatic addition rates differentiate periods of steady-state versus flare-up magmatism in the Central Andean arc. *Communications Earth & Environment* **4** (2023).
4. F. Galetto, Quantification of Subaerial Volcanism and its Products. *EOS* **104** (2023).
5. F. Galetto, M. E. Pritcherd, A. Hornby, E. Gazel, Spatial and Temporal Quantification of Subaerial Volcanism From 1980 to 2019: Solid Products, Masses, and Average Eruptive Rates. *Reviews of Geophysics* **61** (2023).
6. H. Freymuth, M. Brandmeier, G. Wörner, The origin and crust/mantle mass balance of Central Andean ignimbrite magmatism constrained by oxygen and strontium isotopes and erupted volumes. *Contribution to Mineralogy and Petrology* **169** (2015).
7. S. L. de Silva, Altiplano-Puna volcanic complex of the Central Andes. *Geology* **17**, 1102-1106 (1989).
8. S. L. de Silva, S. M. Kay, Turning up the Heat: High-Flux Magmatism in the Central Andes. *Elements* **14**, 245–250 (2018).
9. G. L. Bia, M. G. García, N. J. Cosentino, L. Borgnino, Dispersion of arsenic species from highly explosive historical volcanic eruptions in Patagonia. *Science of the Total Environment* doi:10.1016/j.scitotenv.2022.158389 (2022).
10. L. G. Mastin *et al.*, Multidisciplinary effort to assign realistic source parameters to models of volcanic ash-cloud transport and dispersion during eruptions. *Journal of volcanology and Geothermal Research* **186**, 10-21 (2009).
11. F. Alfano *et al.*, Tephra stratigraphy and eruptive volume of the May, 2008, Chaitén eruption, Chile. *Bulletin of Volcanology*, 1-18 (2010).
12. F. Alfano, C. Bonadonna, P. Delmelle, L. Costantini, Insights on tephra settling velocity from morphological observations. *Journal of Volcanology and Geothermal Research* **208**, 86-98 (2011).
13. A. R. Baker, P. L. Croot, Atmospheric and marine controls on aerosol iron solubility in seawater. *Marine Chemistry* **120**, 4–13 (2008).
14. J. K. Moore, O. Braucher, Sedimentary and mineral dust sources of dissolved iron to the world ocean. *Biogeosciences* **5**, 631-656 (2008).
15. S. M. Kay, B. L. Coira, P. J. Caffe, C.-H. Chen, Regional chemical diversity, crustal and mantle sources and evolution of central Andean Puna plateau ignimbrites. *Journal of Volcanology and Geothermal Research* **198**, 81-111 (2010).
16. N. Olgun *et al.*, Surface ocean iron fertilization: the role of airborne volcanic ash from subduction zone and hot spot volcanoes and related iron fluxes into the Pacific Ocean. *Global Biogeochemical Cycles* **25** (2011).
17. F. Ruggieri *et al.*, Environmental geochemistry of recent volcanic ashes from the Southern Andes. *Environmental Chemistry* **2011**, 236-247 (2011).
18. F. Ruggieri, J. Saavedra, J. L. Fernandez-Turiel, D. Gimeno, M. Garcia-Valles, Environmental geochemistry of ancient volcanic ashes. *Journal of Hazardous materials* **183**, 353-365 (2010).

19. L. E. Simonella *et al.*, Soluble iron inputs to the Southern Ocean through recent andesitic to rhyolitic volcanic ash eruptions from the Patagonian Andes. *Global Biogeochemical Cycles* https://doi.org/10.1002/2015GB005177 (2015).
20. G. Danabasoglu *et al.*, The community earth system model version 2 (CESM2). *Journal of Advances in Modeling Earth Systems* **12**, e2019MS001916 (2020).
21. C. A. Shields *et al.*, The low-resolution CCSM4. *Journal of Climate* **25**, 3993–4014 (2012).
22. C. F. Persch, P. DiNezio, N. S. Lovenduski, The Impact of Orbital Precession on Air-Sea CO2 Exchange in the Southern Ocean. *Geophysical Research Letterrs* **50**, e2023GL103820 (2023).
23. M. C. Long *et al.*, Simulations With the Marine Biogeochemistry Library (MARBL). *Journal of Advances in Modeling Earth Systems* https://doi.org/10.1029/2021MS002647 (2021).
24. G. Danabasoglu *et al.*, The CCSM4 ocean component. *Journal of Climate* **25**, 1361–1389 (2012).
25. P. R. Gent, Effects of southern hemisphere wind changes on the meridional overturning circulation in ocean models. *Annual Review of Marine Science* **8**, 79–94 (2016).
26. N. S. Lovenduski, M. C. Long, P. R. Gent, K. Lindsay, Multi-decadal trends in the advection and mixing of natural carbon in the southern ocean. *Geophysical Research Letters* **40**, 139–142 (2013).
27. R. B. Neale *et al.*, The mean climate of the community atmosphere model (CAM4) in forced SST and fully coupled experiments. *Journal of Climate* **26**, 5150–5168 (2013).
28. N. R. Edwards, R. Marsh, Uncertainties due to transport-parameter sensitivity in an efficient 3-D ocean-climate model. *Climate Dynamics* **24**, 415–433 (2005).
29. A. Ridgwell *et al.*, Marine geochemical data assimilation in an efficient Earth System Model of global biogeochemical cycling. *Biogeosciences* **4**, 87–104 (2007).
30. P. W. Boyd, M. J. Ellwood, The biogeochemical cycle of iron in the ocean. *Nature Geoscience* **3**, 675–682 (2010).
31. K. Matsumoto, T. Tanioka, M. Gilchrist, Sensitivity of Steady State, Deep Ocean Dissolved Organic Carbon to Surface Boundary Conditions. *Global Biogeochemical Cycles* 10.1029/2021GB007102 (2021).
32. A. Tagliabue *et al.*, The integral role of iron in ocean biogeochemistry. *Nature* **543**, 51-59 (2017).
33. S. J. van de Velde, D. Hülse, C. T. Reinhard, A. Ridgwell, Iron and sulfur cycling in the cGENIE.muffin Earth system model (v0.9.21). *Geosci. Model Dev.* **14**, 2713–2745 (2021).
34. J. P. Dunne, J. L. Sarmiento, A. Gnanadesikan, A synthesis of global particle export from the surface ocean and cycling through the ocean interior and on the seafloor. *Global Biogeochemical Cycles* **21** (2007).
35. D. Hülse, A. Ridgwell, Instability in the geological regulation of Earth's climate. *Science* **389** (2025).
36. K. Wallmann, Phosphorus imbalance in the global ocean? . *Global Biogeochemical Cycles* **24** (2010).
37. A. Ridgwell, J. C. Hargreaves, Regulation of atmospheric CO2 by deep-sea sediments in an Earth system model *Global Biogeochemical Cycles* **21** (2007).
38. G. Colbourn, A. Ridgwell, T. M. Lenton, The rock geochemical model (RokGeM) v0. 9. *Geoscientific Model Development* **6**, 1543-1573 (2013).
39. L. Cao *et al.*, The role of ocean transport in the uptake of anthropogenic CO2. *Biogeosciences* **6**, 375–390 (2009).
40. N. M. Mahowald *et al.*, Atmospheric global dust cycle and iron inputs to the ocean *Global biogeochemical cycles* **19** (2005).

41. J. A. Bradley, S. Arndt, Transfer efficiency of organic carbon in marine sediments. *Nature Communications* https://www.nature.com/articles/s41467-022-35112-9 (2022).
42. M. J. Salisbury *et al.*, 40Ar/39Ar chronostratigraphy of Altiplano-Puna volcanic complex ignimbrites reveals the development of a major magmatic province. *GSA Bulletin* **123**, 821-840 (2011).
43. B. Stubbins *et al.*, Global climate forcing on late Miocene establishment of the Pampean aeolian system in South America. *Nature Communications* **14**, 6899 (2023).
44. N. Opazo, N. J. Cosentino, A. Ridgwell, F. Lambert, Sensitivity of Atmospheric Carbon Dioxide to Dust Iron Solubility During the Last Glacial-Interglacial Cycle. *Paleoceanography and Paleoclimatology* doi/10.1029/2025PA005132 (2025).